FootNet: Development of a machine learning emulator of atmospheric transport

Tai-Long He[1#] (taihe@uw.edu)

Nikhil Dadheech[1#] (nd349@uw.edu)

Tammy M. Thompson[2] (tthompson@edf.org)

Alexander J. Turner[1*] (turneraj@uw.edu)

[1]Department of Atmospheric Sciences, University of Washington, Seattle, 98195, WA, USA

[2]Environmental Defense Fund, Boulder, CO, USA

[#]Equally contributed authors

Corresponding author: Alexander J. Turner

FootNet: Development of a machine learning emulator of atmospheric transport

Tai-Long He[1,#], Nikhil Dadheech[1,#], Tammy M. Thompson[2] and Alexander J. Turner[1]

[1]Department of Atmospheric Sciences, University of Washington, Seattle, WA, USA
[2]Environmental Defense Fund, Boulder, CO, USA
[#]Equally contributed authors

Key Points:

- Simulating atmospheric transport at high resolution is becoming a computational bottleneck for estimating emissions with flux inversions
- Trained deep learning models can emulate source-receptor relationships typically constructed with atmospheric transport models
- Deep learning emulators can accelerate construction of source-receptor relationships by ∼7000%, increasing the efficiency of flux inversions

Corresponding author: Alexander J. Turner, `turneraj@uw.edu`

Abstract

There has been a proliferation of dense observing systems to monitor greenhouse gas (GHG) concentrations over the past decade. Estimating emissions with these observations is often done using an atmospheric transport model to characterize the source-receptor relationship, which is commonly termed measurement "footprint". Computing and storing footprints using full-physics models is becoming expensive due to the requirement of simulating atmospheric transport at high resolution. We present the development of FootNet, a deep learning emulator of footprints at kilometer scale. We train and evaluate the emulator using footprints simulated using a Lagrangian particle dispersion model. FootNet predicts the magnitudes and extents of footprints in near-real-time with high fidelity. We identify the relative importance of inputs to FootNet. Surface winds and a precomputed Gaussian plume from the receptor are identified to be the most important variables for footprint emulation. The emulator helps address the computational bottleneck of flux inversions using dense observations.

Plain Language Summary

It is computationally expensive to infer greenhouse gas emissions using atmospheric observations. This is, in part, due to the detailed model used to represent atmospheric transport. This work demonstrates how a machine learning model can be used to accurately simulate high-resolution transport in the atmosphere. This type of machine learning model will help researchers estimate greenhouse gas emissions using densely spaced observations, which are becoming increasingly common with the proliferation of dense urban monitoring networks and geostationary satellites.

1 Introduction

Monitoring anthropogenic greenhouse gas (GHG) emissions is important for ensuring the success of the Paris Agreement's long-term goal on mitigating climate change (IPCC, 2022). To that end, there has been a proliferation of dense observing systems over the past decade to better track GHG emissions. There has been a substantial effort to expand observation networks to better quantify urban GHG emissions, as the majority of the world population lives in urban areas and the degree of urbanization is projected to increase in the future (*World Urbanization Prospects: The 2018 Revision*, 2019). The Northeast Corridor GHG observation network was established to quantify emissions of carbon dioxide and methane using tower-based *in situ* measurements in the highly populated region (Karion et al., 2020). The BErkeley Atmospheric CO_2 Observation Network ($BEACO_2N$; Shusterman et al. (2016)) utilizes low-cost sensors to increase the spatial density of measurements, which could be used to investigate details about urban emissions on intra-city scales. The proliferation of urban GHG observation networks allows for decadal analyses of GHG emissions and provides information to improve the efficiency of GHG reduction policies (Mitchell et al., 2018; Lauvaux et al., 2020). There has been a coincident expansion in satellite GHG observations, which provide similarly dense observations, such as NASA's Orbiting Carbon Observatory-2 (OCO-2) and OCO-3, the TROPOspheric Monitoring Instrument (TROPOMI) onboard the Copernicus Sentinel-5 Precursor (S5P) satellite (Veefkind et al., 2012) for methane, and a planned constellation of GHG monitoring satellites (e.g., GOSAT-GW and MethaneSat).

The increased volume of observational data sets provide more constraints on estimating GHG emissions. However, current methods do not scale well with the incoming observations. The conventional method of inferring GHG emissions using atmospheric observations is done via atmospheric flux inversions (e.g., Jiang et al. (2017); White et al. (2019); Turner et al. (2020)). The state of the of the art in atmospheric flux inversions relies on either Eulerian models or Lagrangian particle dispersion models (LPDMs) to simulate atmospheric transport, which provides the linkage to relate observations to surface fluxes. For example, the four-dimensional variational (4D-Var) method uses the adjoint of Eulerian models to calculate sensitivities of surface fluxes to observations (Baker et al., 2006; Henze et al., 2007; Jiang et al., 2017; Qu et al., 2022). Kalman filters are also widely used in flux inversions, which calculate covariance matrices between prior fluxes and GHG concentrations simulated by Eulerian models to estimate posterior fluxes (Feng et al., 2009; Kang et al., 2011). Alternatively, LPDMs can be used to calculate sensitivity of each observation to its upwind sources by simulating the trajectories of an ensemble of particles advected backward in time (Fasoli et al., 2018; Jones et al., 2007; Pisso et al., 2019). The sensitivity of each receptor to the upwind sources, termed as the receptor's "footprint", can then be used to estimate fluxes inversely (e.g., Turner et al. (2020)). These methods based on full-physics models are becoming prohibitively expensive due to the large computational burden of running high-resolution atmospheric transport models for dense observing systems.

Here we present a deep learning-based emulator, FootNet, to efficiently calculate footprints of ground-based receptors with high fidelity at kilometer-scale spatial resolution. The footprint emulator reduces the computational and storage cost of Lagrangian model-based flux inversion systems by 2–3 orders of magnitude, which will better accommodate the increased volume of GHG observations. We evaluate the performance of the FootNet model using independent data sets. Finally, we assess the relative importance of the features in the machine learning emulator using the permute-and-prediction (PaP) method.

2 Method

2.1 Footprints simulated by the STILT model

Training of the FootNet model is a supervised learning process. This requires ground truth to guide the optimization of the model parameters. Here, we use a full-physics model to generate this ground truth. We simulate footprints using the Stochastic Time-Inverted Lagrangian Transport (STILT) model (Lin et al., 2003; Fasoli et al., 2018), a Lagrangian particle dispersion model (LPDM). The STILT simulations are conducted for two regions: the Barnett Shale region in Texas, and the San Francisco (SF) Bay Area in California (see Figure S1 in Supporting Information). These two regions are chosen because one has simple topography (the Barnett Shale) whereas the other is topographically complex (SF Bay Area). As such, these regions represent limiting cases for the ML model. Further, the combination of two regions will help prevent from overfitting the model to a single location. For the SF Bay Area, STILT simulations are run from 2018 to 2020 with receptors located at realistic sites deployed in the BEACO$_2$N network (see http://beacon.berkeley.edu and Shusterman et al. (2016)). Footprints for the Barnett Shale region are generated from a 1-week WRF-STILT simulation in 2013 (Turner et al., 2018). All footprints are simulated within a 400×400 km^2 domain at 1×1 km^2 spatial resolution.

2.2 Input variables

We use 5 physical parameters from the NOAA High-Resolution Rapid Refresh (HRRR; Benjamin et al. (2016)) model as the input variables, including the 10-meter zonal wind speed (U10M), 10-meter meridional speed (V10M), planetary boundary layer height (PBLH), surface pressure (PRSS), and air density at 850 hPa level (AD850). The FootNet model receives the input variables from the measurement time (t_0) and t_0-6h to predict footprints at t_0. We apply scaling and transformation on the input and output fields to stabilize the training process (see Table S1 in Supporting Information for details). We find that including Gaussian plumes (see Figure 1), calculated using an simple idealized plume model and reversed wind fields, as one of the input variables could significantly improve the performance of FootNet. The Gaussian plume can be efficiently calculated as a Hadamard product from inputs listed above and, as such, adds minimal computational expense. The

Gaussian plume also provides a localization for the ML model in that it tells the ML model where the observation was made and provides an initial guess for what the spatial structure should be. The FootNet model is trained to learn the nonlinear transformation from the idealized Gaussian plumes to footprints using the meteorological fields. The input variables are interpolated to the $400{\times}400$ km^2 domain and the $1{\times}1$ km^2 spatial resolution of footprints.

2.3 Deep learning model and training details

The model structure underlying the footprint emulator is the U-net model (Ronneberger et al., 2015), which is now widely applied in the field of Earth Science (Ghorbanzadeh et al., 2021; He et al., 2022a, 2022b; Zemskova et al., 2022; Tucker et al., 2023). A schematic diagram of the model architecture is shown in Figure 1. The model consists of 4 convolutional blocks and 4 up-convolutional blocks. Each convolutional block includes two convolutional layers with 3×3 convolutional kernels and one 2×2 max-pooling layer. Each up-convolutional layer has one $2{\times}2$ up-convolutional layer followed by two $3{\times}3$ convolutional layers. The convolutional layers are activated by the Rectified Linear Unit (ReLU) function, and are used to capture the spatial patterns hidden in the data. Outputs from the intermediate hidden layers of the model are termed "latent vectors", which is a condensed tensor used by the up-convolutional blocks to predict footprints.

We train and evaluate the emulator using a combined data set with 10,000 footprints from the Barnett Shale and 10,000 footprints from the SF Bay Area. The combined data set is randomly split to 85% as the training data set and 15% as the test data set. The test data set is independent of the training process. 15% of the training data set is used as validation data set to prevent overfitting. We use the mean squared error as the loss function and the Adam optimization algorithm.

2.4 Performance metrics

We evaluate the performance of FootNet using log-transformed footprints to mitigate the impact of the high skewness of the distribution of typical footprint values. The performance of FootNet is assessed using the Intersection-over-Union (IoU) and the Pearson correlation coefficient (r).

IoU measures the accuracy of the area of non-zero footprints predicted by FootNet, which is defined as follows:

$$IoU = \frac{|Y \cap \hat{Y}|}{|Y \cup \hat{Y}|} \tag{1}$$

Here, Y and $\hat{Y}$ stand for the true footprint and the FootNet prediction, respectively. The intersection between Y and $\hat{Y}$ represents the overlapping area of the truth and the prediction, whereas the union represents the area covered by either the truth or the prediction. IoU is used widely to evaluate the ability of deep learning models to make accurately localized predictions.

We calculate correlation coefficients for footprints in the intersection areas between truths and the corresponding predictions, which shows the accuracy in magnitudes of FootNet predictions.

2.5 Permute-and-prediction method

We use the permute-and-prediction (PaP) method to calculate the importance of input variables for footprint emulation, which improves the interpretability of the FootNet model (Fisher et al., 2019). The PaP method estimates variable importance by permuting each input variable with other variables, and the overall accuracy drop represents

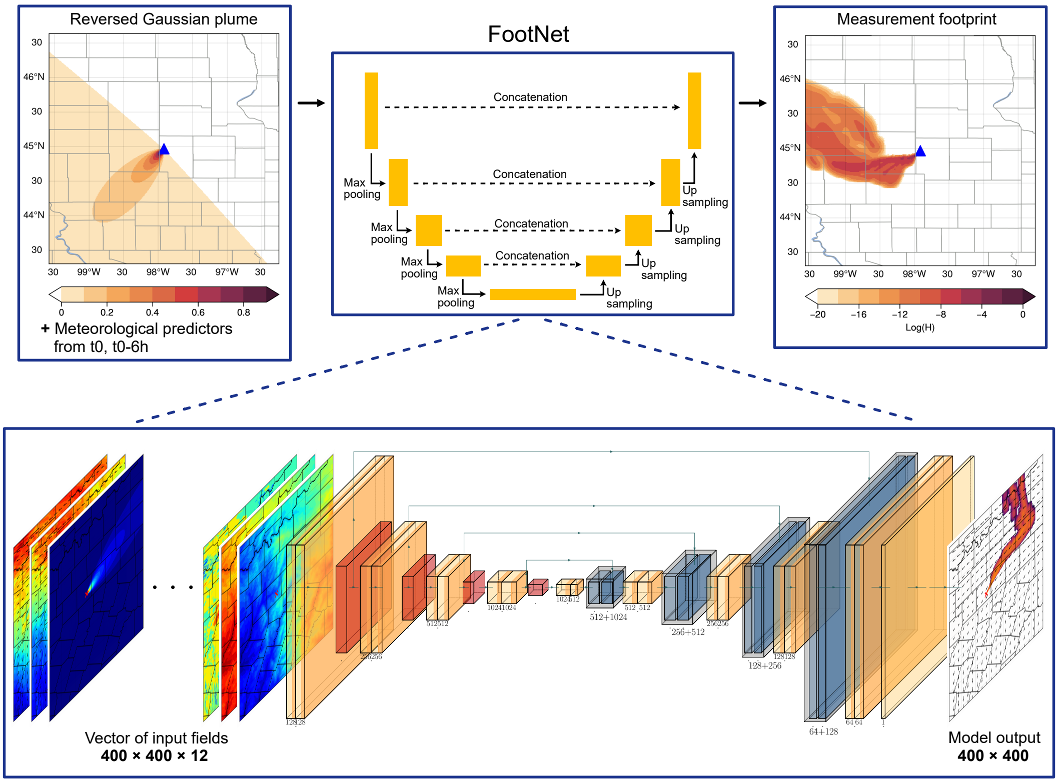

Figure 1. Top row shows the schematic diagram of the FootNet model. Detailed structure of FootNet is shown at the bottom. The orange boxes are 3×3 convolutional layers; the red boxes represent 2×2 max-pooling layers; the light blue boxes are 2×2 transposed convolutional layers. The dark blue boxes represent the latent vectors concatenated from previous layers (shown as the parallel arrows on top).

FootNet's sensitivity to the permuted variable. We estimate variable importance by calculating performance drops in both the IoU and correlation of predicted footprints.

3 Results

3.1 Evaluating performance of the emulator

Figure 2 demonstrates the evolution of FootNet predictions during the training process and the overall performance of FootNet after the training converges. Figure 2D shows a footprint simulated by the STILT model from the test data set, where the footprint is highly nonlinear with a change in direction near the receptor. The corresponding FootNet predictions are shown in Figures 2 (A-C). After iteration A (shortly after the training starts), the FootNet predicts measurement footprints around the receptor with a large negative bias and low correlation coefficient of 0.50. Iteration B is about halfway of the training process, after which the FootNet prediction better captures the general shape of the footprint and the correlation is improved to 0.61. The training stops after iteration C. The final FootNet prediction has enriched details and attains a correlation coefficient of 0.75. Compared to the test data set (i.e, the true footprints from STILT), the IoU of FootNet predictions improves from 0.26 after iteration A to 0.58 after iteration B, and attains a correlation coefficient of 0.76 (see Figure 2A). Figure 2F shows the comparison between the truth and FootNet predictions for all footprints in the test data set.

FootNet predictions show a slight negative bias compared to footprints simulated using the full-physics STILT model. The overall correlation between FootNet predictions and STILT simulations is 0.58.

Figure 3 shows footprints from STILT and FootNet for the two regions: the Barnett Shale and the SF Bay Area. Figures 3A and 3E show results from the simple case (Barnett Shale), where the footprint is similar to an idealized Gaussian plume with time-reversed winds. FootNet well captures both the magnitudes and spatial patterns of the footprint, with an IoU of 0.71 and a correlation coefficient of 0.53. Figures 3B and 3F demonstrate a more complicated meteorological scenario from the Barnett Shale region. The IoU metric and correlation coefficient between the STILT footprint and the FootNet prediction are 0.74 and 0.59, respectively, for this more complex scenario.

Atmospheric transport in the SF Bay Area is decisively more complex as the region includes steep topography, air-sea interactions, and numerous valleys and deltas; Figures 3C and 3D show results from the full-physics model for this region. Emulation of footprints in the SF Bay Area is thus more challenging with an overall degraded fidelity as compared to the Barnett Shale region. Figures 3C and 3G show a receptor with the bulk of the footprint in the Northwest quadrant, these typical meteorological conditions for the SF Bay Area in the summertime with westerly flow bringing airmasses into the SF Bay Area past the Golden Gate Bridge. The shape and the magnitude of the footprint is predicted by FootNet with an IoU of 0.44 and the correlation coefficient to be 0.83. Footprints shown in Figures 3D and 3H show a more complex meteorological scenario. Compared to STILT, the FootNet prediction has an IoU of 0.59 and the correlation is 0.72.

There have been other methods developed to improve the efficiency of footprint calculations. For example, Roten et al. (2021) uses nonlinear weighted averaging to interpolate footprints from locations near the receptors. Fillola et al. (2023) develops a similar footprint emulator based on gradient-boosted regression trees (GBRTs), at a coarse spatial resolution (20–30 km in mid-latitudes) and 10 grid cells around the measurement location. The FootNet model reproduces the full-physics model with high fidelity at high-resolution. This is impressive given the complex topography and meteorology of the regions studied here could complicate the emulation of footprints due to their impact on transport at kilometer scale. FootNet only takes meteorological fields and the idealized Gaussian plume as its input. No additional LPDM simulations are needed to generate footprint predictions after the training process.

Using the full-physics STILT model, it takes about 6 months to run 10^8 particle trajectories for the computation of 1 week of hourly footprints at kilometer scale. The storage requirement also makes it impractical to use the full-physics model with dense observations, as the computed 1-week hourly footprints would require 4-terabyte storage space for future re-use. Emulation of footprints using the FootNet model addresses these two issues and facilitates LPDM-based flux inversion systems with dense observing systems. The generation of each footprint prediction takes $\sim$1 s on central processing units (CPUs), which can be further reduced to 0.08 s on a graphics processing units (GPU). To analyze a single day of observations made at the 40 BEACO$_2$N sites in the SF Bay Area (approx. 650 observations per day), it takes the STILT model 2 hours on 10 compute nodes with 32 CPU cores to generate the required footprints, whereas only 6 min is required for FootNet on one GPU node. This computational efficiency of the approach mitigates the storage requirement, as footprints could be generated by FootNet in near real-time and there is no need to storage the computed footprints.

3.2 Importance of input variables

Figure 4 shows the ranking of variable importance for FootNet calculated using the PaP method. We group variable importance by variable names and time steps. The most

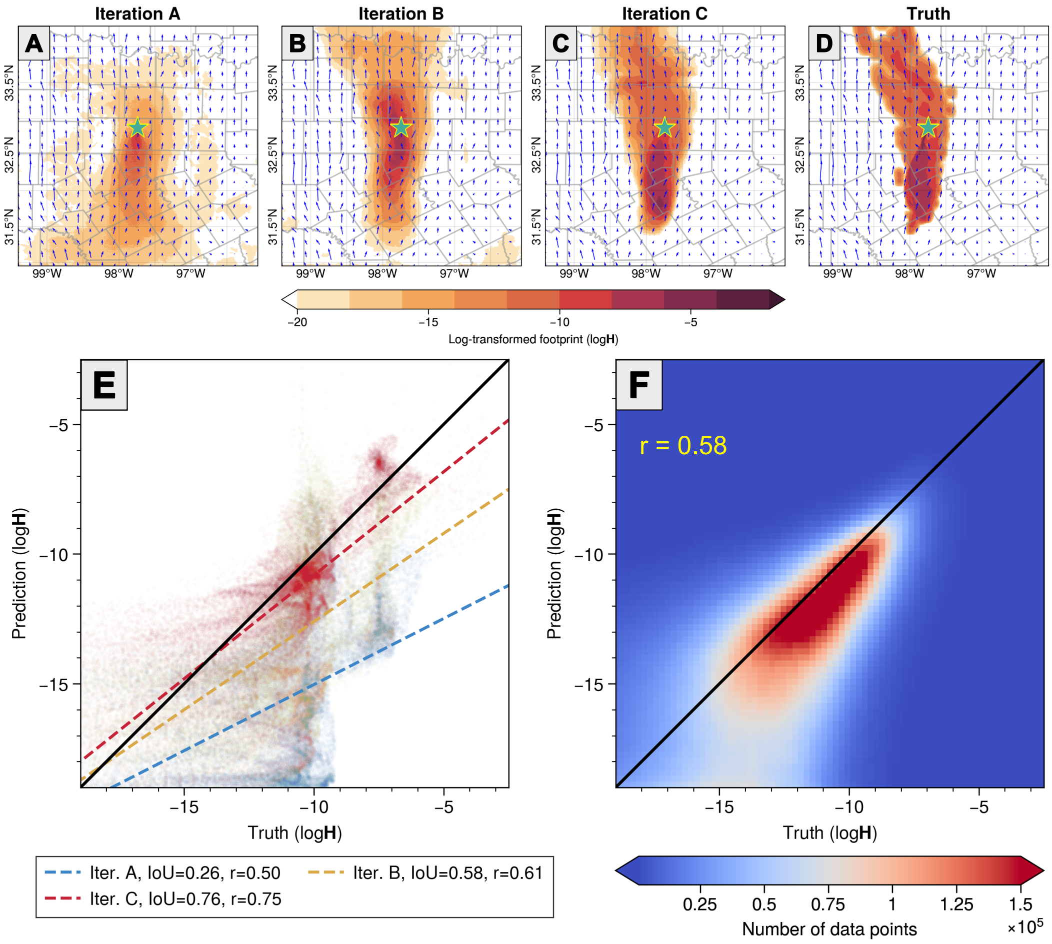

Figure 2. Convergence of the training process and evaluation of the model performance on the independent test data set. (A-C) FootNet predictions from three stages in the training process, corresponding to the truth in (D). The blue arrows represent wind vectors, and the green stars show the location of the receptors. (E) Comparison between footprints simulated by STILT and FootNet predictions in (A-C). (F) Comparison between FootNet and STILT for all footprints in the test data set.

important meteorological variables are the 10-meter wind speeds, which lead to a ∼0.4 decrease in correlation and the IoU drops by ∼0.16. Permuting Gaussian plumes degrades the IoU of correlation of FootNet predictions by 0.25 and 0.1, respectively. FootNet is less sensitive to surface pressure and air density at 850 hPa than other input variables, and planetary boundary layer height shows the lowest variable importance. Meteorological variables from different time steps show similar importance for footprint emulation. The IoU is more sensitive to meteorological variables from $t_0 - 6h$, whereas information from the measurement time (t_0) is more important for the magnitude accuracy of FootNet predictions.

PaP method provides a rough estimate of variable importance, this is because the inter-correlation between input variables can lead to an inflation of the feature importance (Hooker et al., 2021). Nevertheless, the calculated variable importance is in alignment with with our understanding about the calculation of source-receptor footprints. Namely, that the computation of footprints with a full-physics model requires advecting particles with the precomputed wind fields, the PaP method indicates the importance of this in the ML model by identifying the 10-m winds as the most important parameters. The Gaussian plume is also identified as highly important. This is, again, because the Gaussian plume is the only input field that provides information about the location of the observational receptor location.

4 Conclusions

Here we described the developed a machine learning emulator of surface measurement footprints, FootNet. This machine learning model can be used to improve the computational efficiency of high-resolution greenhouse gas flux . The FootNet model was trained and evaluated using footprints simulated by the STILT full-physics model for the SF Bay Area and the Barnett Shale region. We show the FootNet prediction evolves and converges to the STILT truth as the training iterates. The overall correlation between FootNet predictions and the STILT simulations is 0.58. The footprint emulator well predicts both the shapes of magnitudes of footprints with a high fidelity. We calculate variable importance for FootNet using the PaP method to improve the interpretability of the FootNet model. 10-meter wind speeds and Gaussian plumes have the greatest importance for the emulation of footprints. The emulation of footprints using FootNet is computationally efficient and mitigates the burden of storing footprints for each measurement location, which makes it feasible to deliver high-resolution estimates of GHG fluxes in near real-time using proliferated dense observing systems in the future.

5 Open Research

We use the full-physics Stochastic Time-Inverted Lagrangian Transport Model (STILT) to simulation footprints for the training of FootNet. The STILT model could be accessed from `https://uataq.github.io/stilt/` (Fasoli et al., 2018). The footprints simulated by the STILT model are available through Turner et al. (2018) and Turner et al. (2020). Examples of the footprint data sets used in the training process could be downloaded from `https://hermes.atmos.washington.edu/footnet_training_samples/footprints_data.tar.gz`. The meteorological variables are from the High-Resolution Rapid Refresh (HRRR) data product, which is available at `https://rapidrefresh.noaa.gov/hrrr/` (Dowell et al., 2022; James et al., 2022). The repository of the code used in the manuscript is publicly available at `https://github.com/tailonghe/FootNet_tf/`.

Acknowledgments

This work is supported by a NASA Early Career Faculty Grant (80NSSC21K1808) to A.J.T. and NASA FINESST Grant (80NSSC22K1557) to N.D. We acknowledge funding from Environmental Defense Fund, whose work is supported by gifts from Signe Ostby, Scott Cook and Valhalla Foundation. This work is supported in part by the generosity of Eric and Wendy Schmidt by recommendation of Schmidt Futures, as part of its Virtual Earth System Research Institute (VESRI).

The authors declare no conflict of interest.

References

Baker, D. F., Doney, S. C., & Schimel, D. S. (2006). Variational data assimilation for atmospheric co2. *Tellus B: Chemical and Physical Meteorology*, *58*(5), 359-365. Retrieved from `https://doi.org/10.1111/j.1600-0889.2006.00218.x` doi: 10.1111/j.1600-0889.2006.00218.x

Benjamin, S. G., Weygandt, S. S., Brown, J. M., Hu, M., Alexander, C. R., Smirnova, T. G., … Manikin, G. S. (2016). A north american hourly assimilation and model forecast cycle: The rapid refresh. *Monthly Weather Review*, *144*(4), 1669 - 1694. Retrieved from https://journals.ametsoc.org/view/journals/mwre/144/4/mwr-d-15-0242.1.xml doi: https://doi.org/10.1175/MWR-D-15-0242.1

Dowell, D. C., Alexander, C. R., James, E. P., Weygandt, S. S., Benjamin, S. G., Manikin, G. S., ... Alcott, T. I. (2022). The high-resolution rapid refresh (hrrr): An hourly updating convection-allowing forecast model. part i: Motivation and system description. *Weather and Forecasting*, *37*(8), 1371 - 1395. Retrieved from https://journals.ametsoc.org/view/journals/wefo/37/8/WAF-D-21-0151.1.xml doi: https://doi.org/10.1175/WAF-D-21-0151.1

Fasoli, B., Lin, J. C., Bowling, D. R., Mitchell, L., & Mendoza, D. (2018). Simulating atmospheric tracer concentrations for spatially distributed receptors: updates to the stochastic time-inverted lagrangian transport model's r interface (stilt-r version 2). *Geoscientific Model Development*, *11*(7), 2813–2824. Retrieved from https://gmd.copernicus.org/articles/11/2813/2018/ doi: 10.5194/gmd-11-2813-2018

Feng, L., Palmer, P. I., Bösch, H., & Dance, S. (2009). Estimating surface co_2 fluxes from space-borne co_2 dry air mole fraction observations using an ensemble kalman filter. *Atmospheric Chemistry and Physics*, *9*(8), 2619–2633. Retrieved from https://acp.copernicus.org/articles/9/2619/2009/ doi: 10.5194/acp-9-2619-2009

Fillola, E., Santos-Rodriguez, R., Manning, A., O'Doherty, S., & Rigby, M. (2023). A machine learning emulator for lagrangian particle dispersion model footprints: a case study using name. *Geoscientific Model Development*, *16*(7), 1997–2009. Retrieved from https://gmd.copernicus.org/articles/16/1997/2023/ doi: 10.5194/gmd-16-1997-2023

Fisher, A., Rudin, C., & Dominici, F. (2019, 01). All models are wrong, but many are useful: Learning a variable's importance by studying an entire class of prediction models simultaneously. *Journal of machine learning research : JMLR*, *20*.

Ghorbanzadeh, O., Crivellari, A., Ghamisi, P., Shahabi, H., & Blaschke, T. (2021, Jul 16). A comprehensive transferability evaluation of u-net and resu-net for landslide detection from sentinel-2 data (case study areas from taiwan, china, and japan). *Scientific Reports*, *11*(1), 14629. Retrieved from https://doi.org/10.1038/s41598-021-94190-9 doi: 10.1038/s41598-021-94190-9

He, T.-L., Jones, D. B. A., Miyazaki, K., Bowman, K. W., Jiang, Z., Chen, X., ... Li, K. (2022b). Inverse modelling of chinese no_x emissions using deep learning: integrating in situ observations with a satellite-based chemical reanalysis. *Atmospheric Chemistry and Physics*, *22*(21), 14059–14074. Retrieved from https://acp.copernicus.org/articles/22/14059/2022/ doi: 10.5194/acp-22-14059-2022

He, T.-L., Jones, D. B. A., Miyazaki, K., Huang, B., Liu, Y., Jiang, Z., ... Worden, J. R. (2022a). Deep learning to evaluate us nox emissions using surface ozone predictions. *Journal of Geophysical Research: Atmospheres*, *127*(4), e2021JD035597. Retrieved from https://agupubs.onlinelibrary.wiley.com/doi/abs/10.1029/2021JD035597 (e2021JD035597 2021JD035597) doi: https://doi.org/10.1029/2021JD035597

Henze, D. K., Hakami, A., & Seinfeld, J. H. (2007). Development of the adjoint of geos-chem. *Atmospheric Chemistry and Physics*, *7*(9), 2413–2433. Retrieved from https://acp.copernicus.org/articles/7/2413/2007/ doi: 10.5194/acp-7-2413-2007

Hooker, G., Mentch, L., & Zhou, S. (2021). *Unrestricted permutation forces extrapolation: Variable importance requires at least one more model, or there is no free variable importance.*

IPCC. (2022). *Global warming of 1.5°c: Ipcc special report on impacts of global* *warming of 1.5°c above pre-industrial levels in context of strengthening response to climate change, sustainable development, and efforts to eradicate poverty.* Cambridge University Press. doi: 10.1017/9781009157940

James, E. P., Alexander, C. R., Dowell, D. C., Weygandt, S. S., Benjamin, S. G., Manikin, G. S., ... Turner, D. D. (2022). The high-resolution rapid refresh (hrrr): An hourly updating convection-allowing forecast model. part ii: Forecast performance. *Weather and Forecasting*, *37*(8), 1397 - 1417. Retrieved from `https://journals.ametsoc.org/view/journals/wefo/37/8/WAF-D-21-0130.1.xml` doi: https://doi.org/10.1175/WAF-D-21-0130.1

Jiang, Z., Worden, J. R., Worden, H., Deeter, M., Jones, D. B. A., Arellano, A. F., & Henze, D. K. (2017). A 15-year record of co emissions constrained by mopitt co observations. *Atmospheric Chemistry and Physics*, *17*(7), 4565–4583. Retrieved from `https://acp.copernicus.org/articles/17/4565/2017/` doi: 10.5194/acp-17-4565-2017

Jones, A., Thomson, D., Hort, M., & Devenish, B. (2007). The u.k. met office's next-generation atmospheric dispersion model, name iii. In C. Borrego & A.-L. Norman (Eds.), *Air pollution modeling and its application xvii* (pp. 580–589). Boston, MA: Springer US.

Kang, J.-S., Kalnay, E., Liu, J., Fung, I., Miyoshi, T., & Ide, K. (2011). "variable localization" in an ensemble kalman filter: Application to the carbon cycle data assimilation. *Journal of Geophysical Research: Atmospheres*, *116*(D9). Retrieved from `https://agupubs.onlinelibrary.wiley.com/doi/abs/10.1029/2010JD014673` doi: https://doi.org/10.1029/2010JD014673

Karion, A., Callahan, W., Stock, M., Prinzivalli, S., Verhulst, K. R., Kim, J., ... Whetstone, J. (2020). Greenhouse gas observations from the northeast corridor tower network. *Earth System Science Data*, *12*(1), 699–717. Retrieved from `https://essd.copernicus.org/articles/12/699/2020/` doi: 10.5194/essd-12-699-2020

Lauvaux, T., Gurney, K. R., Miles, N. L., Davis, K. J., Richardson, S. J., Deng, A., ... Turnbull, J. (2020). Policy-relevant assessment of urban co2 emissions. *Environmental Science & Technology*, *54*(16), 10237-10245. Retrieved from `https://doi.org/10.1021/acs.est.0c00343` (PMID: 32806908) doi: 10.1021/acs.est.0c00343

Lin, J. C., Gerbig, C., Wofsy, S. C., Andrews, A. E., Daube, B. C., Davis, K. J., & Grainger, C. A. (2003). A near-field tool for simulating the upstream influence of atmospheric observations: The stochastic time-inverted lagrangian transport (stilt) model. *Journal of Geophysical Research: Atmospheres*, *108*(D16). Retrieved from `https://agupubs.onlinelibrary.wiley.com/doi/abs/10.1029/2002JD003161` doi: https://doi.org/10.1029/2002JD003161

Mitchell, L. E., Lin, J. C., Bowling, D. R., Pataki, D. E., Strong, C., Schauer, A. J., ... Ehleringer, J. R. (2018). Long-term urban carbon dioxide observations reveal spatial and temporal dynamics related to urban characteristics and growth. *Proceedings of the National Academy of Sciences*, *115*(12), 2912-2917. Retrieved from `https://www.pnas.org/doi/abs/10.1073/pnas.1702393115` doi: 10.1073/pnas.1702393115

Pisso, I., Sollum, E., Grythe, H., Kristiansen, N. I., Cassiani, M., Eckhardt, S., ... Stohl, A. (2019). The lagrangian particle dispersion model flexpart version 10.4. *Geoscientific Model Development*, *12*(12), 4955–4997. Retrieved from `https://gmd.copernicus.org/articles/12/4955/2019/` doi: 10.5194/gmd-12-4955-2019

Qu, Z., Henze, D. K., Worden, H. M., Jiang, Z., Gaubert, B., Theys, N., & Wang, W. (2022). Sector-based top-down estimates of nox, so2, and co emissions in east asia. *Geophysical Research Letters*, *49*(2), e2021GL096009. Retrieved from `https://agupubs.onlinelibrary.wiley.com/doi/abs/10.1029/2021GL096009` (e2021GL096009 2021GL096009) doi: https://doi.org/10.1029/

2021GL096009

Ronneberger, O., Fischer, P., & Brox, T. (2015). U-Net: Convolutional Networks for Biomedical Image Segmentation. In N. Navab, J. Hornegger, W. M. Wells, & A. F. Frangi (Eds.), *Medical Image Computing and Computer-Assisted Intervention – MICCAI 2015* (pp. 234–241). Cham: Springer International Publishing. doi: 10.1007/978-3-319-24574-4_28

Roten, D., Wu, D., Fasoli, B., Oda, T., & Lin, J. C. (2021). An interpolation method to reduce the computational time in the stochastic lagrangian particle dispersion modeling of spatially dense xco2 retrievals. *Earth and Space Science*, *8*(4), e2020EA001343. Retrieved from https://agupubs.onlinelibrary.wiley.com/doi/abs/10.1029/2020EA001343 (e2020EA001343 2020EA001343) doi: https://doi.org/10.1029/2020EA001343

Shusterman, A. A., Teige, V. E., Turner, A. J., Newman, C., Kim, J., & Cohen, R. C. (2016). The berkeley atmospheric co_2 observation network: initial evaluation. *Atmospheric Chemistry and Physics*, *16*(21), 13449–13463. Retrieved from https://acp.copernicus.org/articles/16/13449/2016/ doi: 10.5194/acp-16-13449-2016

Tucker, C., Brandt, M., Hiernaux, P., Kariryaa, A., Rasmussen, K., Small, J., ... Fensholt, R. (2023, Mar 01). Sub-continental-scale carbon stocks of individual trees in african drylands. *Nature*, *615*(7950), 80-86. Retrieved from https://doi.org/10.1038/s41586-022-05653-6 doi: 10.1038/s41586-022-05653-6

Turner, A. J., Jacob, D. J., Benmergui, J., Brandman, J., White, L., & Randles, C. A. (2018). Assessing the capability of different satellite observing configurations to resolve the distribution of methane emissions at kilometer scales. *Atmospheric Chemistry and Physics*, *18*(11), 8265–8278. Retrieved from https://acp.copernicus.org/articles/18/8265/2018/ doi: 10.5194/acp-18-8265-2018

Turner, A. J., Kim, J., Fitzmaurice, H., Newman, C., Worthington, K., Chan, K., ... Cohen, R. C. (2020). Observed impacts of covid-19 on urban co2 emissions. *Geophysical Research Letters*, *47*(22), e2020GL090037. Retrieved from https://agupubs.onlinelibrary.wiley.com/doi/abs/10.1029/2020GL090037 (e2020GL090037 10.1029/2020GL090037) doi: https://doi.org/10.1029/2020GL090037

Veefkind, J., Aben, I., McMullan, K., Förster, H., de Vries, J., Otter, G., ... Levelt, P. (2012). Tropomi on the esa sentinel-5 precursor: A gmes mission for global observations of the atmospheric composition for climate, air quality and ozone layer applications. *Remote Sensing of Environment*, *120*, 70-83. Retrieved from https://www.sciencedirect.com/science/article/pii/S0034425712000661 (The Sentinel Missions - New Opportunities for Science) doi: https://doi.org/10.1016/j.rse.2011.09.027

White, E. D., Rigby, M., Lunt, M. F., Smallman, T. L., Comyn-Platt, E., Manning, A. J., ... Palmer, P. I. (2019). Quantifying the uk's carbon dioxide flux: an atmospheric inverse modelling approach using a regional measurement network. *Atmospheric Chemistry and Physics*, *19*(7), 4345–4365. Retrieved from https://acp.copernicus.org/articles/19/4345/2019/ doi: 10.5194/acp-19-4345-2019

World urbanization prospects: The 2018 revision. (2019). United Nations.

Zemskova, V. E., He, T.-L., Wan, Z., & Grisouard, N. (2022, Jul 13). A deep-learning estimate of the decadal trends in the southern ocean carbon storage. *Nature Communications*, *13*(1), 4056. Retrieved from https://doi.org/10.1038/s41467-022-31560-5 doi: 10.1038/s41467-022-31560-5

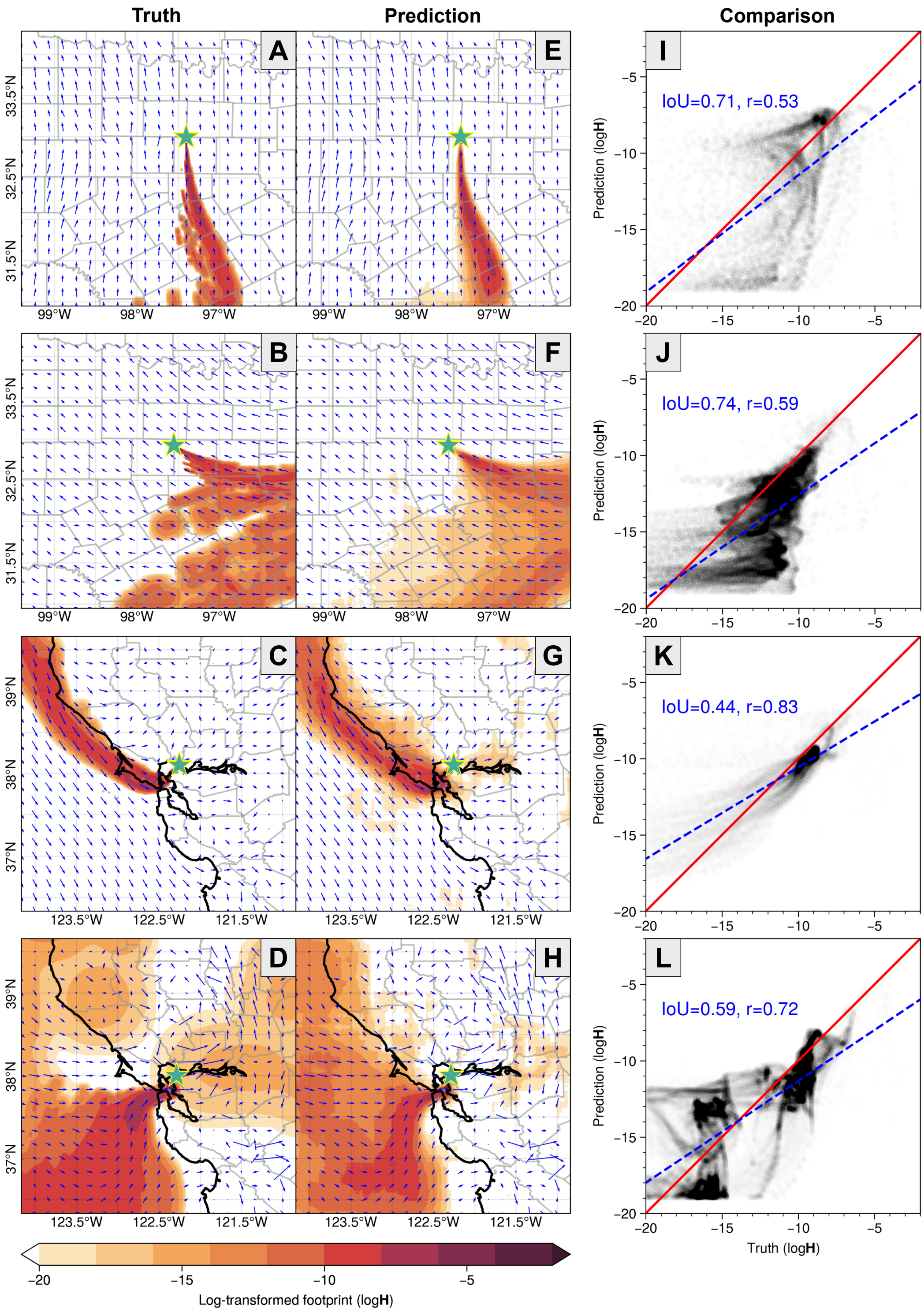

Figure 3. Evaluation of individual FootNet predictions for the test data set. (A-D) Footprints simulated by the full-physics STILT model for the Barnett Shale region and the SF Bay Area, which are treated as the truth in the training process. (E-H) Footprint predictions made by FootNet corresponding to (A-D). The blue arrows represent wind vectors, and the green stars show the location of the receptors. (I-L) Comparison and correlation between the truths and predictions for the four examples.

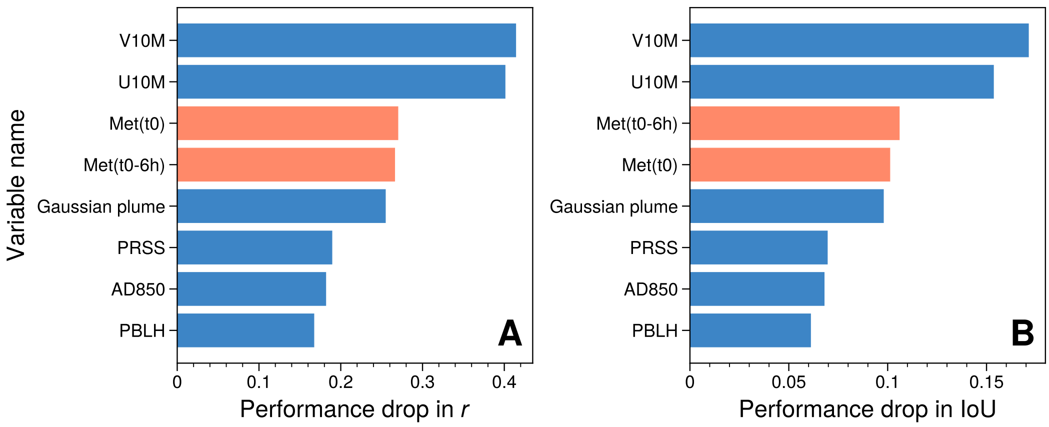

Figure 4. Rankings of importance of the input variables estimated using the permute-and-predict (PaP) method. (A) Performance drop in the correlation coefficients after permuting the input variables.